MEASUREMENTS OF PLASMA CONFINEMENT

THE 10 METER MULTIPLE-MIRROR EXPERIMENT

by

H. D. Price, A. J. Lichtenberg, M. A. Lieberman and M. Tuzsewski

MEASUREMENTS OF PLASMA CONFINEMENT
THE 10 METER MULTIPLE-MIRROR EXPERIMENT

H. D. Price, A. J. Lichtenberg and M. A. Lieberman

Department of Electrical Engineering and Computer Sciences
and the Electronics Research Laboratory
University of California, Berkeley, California 94720

and

M. Tuszewski

Los Alamos Scientific Laboratory, Los Alamos, New Mexico

ABSTRACT

Plasma confinement is studied experimentally in the Berkeley 10 Meter Multiple-Mirror Device (MMX). Stability is achieved by a set of linked quadrupoles which produce an average minimum-B field configuration. Mirror ratios are varied between $M = 2$ and 4 and the midplane field strengths varied between $B_0 = 1.1$ and 2.1 kG. A conical theta-pinch produces a hydrogen plasma with an initial temperature $T_i = T_e \sim 8$ eV and with an initial axial density profile heavily weighted in the first half of the system (with peak amplitude $n \sim 10^{15}$ cm^{-3}). Dual injection (with a Marshall gun at the opposite end) fills the device in a more symmetric manner. A longitudinal array of Langmuir probes follows the density variation in space and time from the high density regime dominated by radial loss through the diffusive multiple-mirror regime in which both radial and axial losses are important. The observed confinement times are predicted reasonably well by an analytic estimate and by a numerical simulation. Each calculation accounts for axial and radial loss due to classical processes only, with the radial diffusion enhanced by the highly eccentric elliptical flux surfaces. A multiple-mirror normal mode is achieved with center cell density in the range $n \approx 10^{12}$ cm^{-3}, with axial profiles in qualitative agreement with those predicted by the numerical simulation. The results indicate that the confinement in a stabilized multiple mirror is governed by classical collisions alone.

I. INTRODUCTION

Plasma confinement in a multiple-mirror field has been previously investigated at Berkeley in a 7 cell, 2 meter long device. Both steady-state [1] and transient [2] experiments were performed. The plasma was stabilized by a set of linked quadrupoles which reduced but did not reverse the average magnetic field curvature. Peak beta was less than 1 percent and the decay in the high-density MHD flow regime was not investigated in these studies.

In the 10 meter device [3] described in Section 2 of this paper the plasma temperature and density are scaled to higher values while keeping the mean-free-path $\lambda_{ii} \alpha \, \ell_c$, the cell length is also increased so that $\ell_c \gg \ell_m$, where ℓ_m is the magnetic mirror scale length. Peak beta values in the center of the device exceed 10 percent. The magnetic field coils produce a shallow average minimum-B well which is optimized to maximize the well radius while minimizing the flux surface ellipticity at the mirror throats [4]. The increased cell length permits full development of the normal modes which are characteristic of the higher-intermediate density regime ($\lambda_{ii}/M < \ell_m$, where M is the mirror ratio). These modes were never completely established in the previous experiments conducted in the 2 meter device. The evolution of the density decay through the lower-intermediate regime ($\ell_c < \lambda_{ii}/M < L$, where L is the system length) and into the free flow regime ($\lambda_{ii} \sim L$) may also be followed.

Section 2 describes the experimental set-up. Section 3 discusses the theoretical assumption for calculating the confinement time, and describes briefly a numerical model, only classical losses are included, but the effects of both like and unlike particle collisions are

incorporated into the radial diffusion. The enhancement of the radial loss due to the strong transverse density gradients produced by the elliptical flux surfaces is also included. Ambipolar effects on the axial diffusion are included in the numerical model. Experiment and theory are compared in Section 4 and discrepancies are discussed in Section 5.

2. EXPERIMENTAL SET-UP

It was originally intended that the theta-pinch be the only source of plasma for the experiment. However, it was found that when operating in this mode the initial longitudinal density profile was heavily weighted toward the source end of the device due to a combination of trapping, expansion and radial loss in the first few cells. A symmetric filling (with $n(z,t_0)$ nearly uniform in z) was desired (but not necessary) to make the experiment more compatible with existing theoretical models.

To achieve a more uniform filling a Marshall gun was installed at the end opposite the theta-pinch (see Fig. 1(a)). Each injector was fed a puff of hydrogen gas by identical fast acting pulsed valves. Each source injects a plasma into a solenoidal guide field region. The mirror coil nearest the Marshall gun at throat T_{10} was removed from the mirror circuit for these measurements. Residual neutral gas was thereby eliminated by time of flight separation. Circular graphite apertures were installed in each guide field to define and center the plasma and to remove the plasma from the regions near the stainless steel vacuum vessel walls. With this scheme it was possible to produce an initial center cell density and temperature of $n \sim 10^{14}$ cm^{-3} and $T_e \sim 8$ eV. (These parameters place the ion-ion mean-free-path in the MHD regime $\lambda_{ii} \ll \ell_m$.)

The sources, solenoidal coils, and mirror coils are shown schematically in Fig. 1(a) and the axial magnetic field profile is shown in Fig. 1(b). Nine mirror cells, each of length ℓ_c = 75 cm are bounded by mirror throats T_0, T_1, ..., T_9. With this configuration the center of the device is the midplane between mirror throats 4 and 5 (M_{45}).

Stabilization of interchange modes is provided by two sets of linked quadrupole coils [4]. The weak quadrupoles run along an entire cell, reversing polarity at the mirrors. They produce "weakly-good" fieldline curvature throughout most of the cell length. The strong quadrupoles are localized about each mirror and produce the strong stabilizing curvature necessary to counter the effect of the mirror coils. Together these coils yield a vacuum magnetic field for which $\int \frac{d\ell}{B} < 0$ (out to some critical midplane radius).

The quadrupole field in each of the end guide field regions (composed of both strong and weak transition quadrupoles) is designed to map a set of fieldlines defined by the circular aperture into elliptical cross sections at the mirror throats and circles at the cell midplanes. The experiments were performed at mirror ratios M = 2,3 and 4 for which the corresponding flux surface ellipticities (at the mirror throats) necessary for stabilization are 10, 18 and 25. In Fig. 2 a section of the flux surfaces in the first two cells is shown together with photographs of the flux surface cross sections taken with a plasma camera and using an electron beam source located in the theta-pinch guide field. The solenoidal magnetic field strength was varied discretely between low, intermediate and high peak valves of 1.4, 2.1 and 2.8 kG. The solenoidal, mirror, strong and weak quadropole currents are provided by four separate

capacitor banks, with the currents rising in ~ 200-500 μs and decaying in ~ 2 ms.

3. ANALYTICAL AND NUMERICAL CALCULATIONS

A modified version of the simulation model and a portion of the theoretical basis for the analytical calculation used here has been described in a previous paper [2].

The ion density continuity equation may be written:

$$\frac{\partial n}{\partial t} = \nabla \cdot (\underline{\Gamma}_{\parallel} + \underline{\Gamma}_{\perp}) \tag{1}$$

indicating that plasma particles escape both axially and radially. Here $\underline{\Gamma}_{\parallel}$ is the axial particle flux and $\underline{\Gamma}_{\perp}$ is the radial particle flux. The nature of the axial particle confinement depends upon the relationship between the ion-ion mean-free-path λ_{ii} and the cell length ℓ_c. Three regimes may be distinguished: (1) MHD (high density), (2) multiple-mirror (intermediate density) and (3) free-flow (low density).

Axial loss times in the high density MHD flow regime scale as τ_{MHD} ~ $m(\frac{L}{2v})$, where v is the ion thermal speed. This expression is a single-cell transit time modified by a self-mirroring effect [5]. This situation is realized when the mean free path is much less than the mirror scale length $(\lambda_{ii} \ll \ell_m, \; \ell_m^{-1} = \frac{1}{B_z} \frac{dB_z}{dz})$.

Plasma parameters fall into the multiple-mirror regime when the mean-free-path for ions to scatter into a loss cone angle is comparable to a cell length $(\lambda_{ii}/M \sim \ell_c)$. Two subregimes may be distinguished. In the higher-intermediate density regime $(\lambda_{ii}/M < \ell_c)$ single-particle axial motion is characterized by a random walk of constant step length

-4-

equal to the cell length ℓ_c. After several decay times the system would be expected to exhibit a convex cosine-like axial normal mode. In the lower-intermediate density regime ($\ell_c < \lambda_{ii}/M < L$) the axial diffusion step length is the ion mean-free-path, which is density dependent. Solutions to the continuity equation for the ion density can possess regions along the z axis convex (near the device center) and concave (near the ends). Multiple-mirror loss times are given approximately as [6]: $\tau_{mm} = \frac{kM}{\rho(M)} \left(\frac{L}{2v}\right)$, where k is the number of mirror cells and $\rho(M)$ is of order unity, and accounts for an average over an assumed Maxwellian velocity distribution at a given mirror ratio M. This expression makes evident the strong enhancement in confinement over that in the MHD and free-flow regimes. The diffusive L^2 scaling (putting $k = L/\ell_c$) is in contrast to the usual scaling with L characteristic of MHD flow.

As the decay proceeds in time, the mean-free-path falls into the low density, free-flow regime ($\lambda_{ii}/M \geq L$) for which particles that scatter into the loss cone are lost axially in a transit time ($L/2v$). This regime is characterized by an n(z,t) which flattens with increasing time until the density is axially uniform.

In the following, only classical radial losses are accounted for, with both the electron-ion term and the ion-ion term, which becomes significant in the presence of strong radial density gradients [7] are included. Explicitly

$$\Gamma_{ei} = D_{ei} \nabla_\perp n \tag{2a}$$

$$\Gamma_{ii} = A\nabla_\perp [n^2 \nabla_\perp (\frac{1}{n} \nabla_\perp n)]. \tag{2b}$$

The subscripts ei and ii specify the losses as due to unlike or like particle collisions respectively. In the above, D_{ei} is the usual classical electron-ion diffusion coefficient: $D_{ei} = a_e^2 \mu_{ei}$ (with a_e the electron gyroradius and μ_{ei} the electron-ion collision frequency) and $A = \frac{3}{8} \frac{a_i^4}{n\tau_{ii}}$ (with a_i the ion gyroradius and τ_{ii} the 90° ion-ion scattering time). From Eq. (1), if the density is assumed uniform along the axis of the entire system, then the total confinement time may be decomposed as

$$\frac{1}{\tau} = \frac{1}{\tau_\parallel} + \frac{1}{\tau_\perp} \quad \left(\text{with } \frac{1}{\tau_\perp} = \frac{1}{\tau_{\perp ei}} + \frac{1}{\tau_{\perp ii}}\right), \tag{3}$$

where $\tau_\parallel$ and $\tau_\perp$ are the characteristic axial and radial times. In this spirit, axial and radial loss rates are calculated independently and combined to yield a total decay time.

Radial loss rates depend critically on the flux surface shapes, which change continuously along the axis. To calculate a global time constant it is appropriate to average Eq. (2) over the plasma boundary in a given cell. If the local mirror ratio is defined as: $M(z) = B(z)/B_0$ and x_p is chosen to denote the characteristic plasma radial scale length, then with the aid of Eqs. (2a) and (2b) Eq. (3) may be rewritten

$$\frac{1}{\tau_\perp} = \frac{A_{ei}}{\tau_{\perp ei0}} + \frac{A_{ii}}{\tau_{\perp ii0}} \tag{4a}$$

with,

$$A_{ei} = \frac{1}{2\pi \ell_c} \iint \frac{d\theta dz}{(x_p/x_{p0})^2 M^2} \qquad A_{ii} = \frac{1}{2\pi \ell_c} \iint \frac{d\theta dz}{(x_p/x_{p0})^4 M^4}$$

and,

$$\tau_{\perp ei0} = \frac{x_{p0}^2}{D_{ei0}} = (\frac{m_i}{m_e})^{1/2} (\frac{x_{p0}}{a_{i0}})^2 (\frac{T_e}{T_i})^{1/2} \tau_{ii0} \tag{4b}$$

$$\tau_{\perp ii0} = \frac{1}{2}(\frac{x_{p0}}{a_{i0}})^4 \tau_{ii0} \tag{4c}$$

From previous numerical work [7] the computed ion-ion radial loss flux was found to be higher than that predicted from the above analysis by a factor between 6 (for a slab) and 4 (for a circular cross section). For this reason Eq. (4) includes an ad hoc multiplicative factor of 1/5.

Equation (4a) indicates that under this averaging scheme it is possible to express the global radial loss rate in a given cell in terms of local plasma parameters evaluated at the midplane weighted by certain integrals of field quantities. If it is further assumed that $x_p(\theta,z) \sim (x_p(z))_{min}$ then with flux conservation it may be shown that:

$$A_{ei} = \frac{1}{\ell_c} \int_0^{\ell_c} (\frac{Q}{M})dz \tag{5a}$$

$$A_{ii} = \frac{1}{\ell_c} \int_0^{\ell_c} (\frac{Q}{M})^2 dz \tag{5b}$$

where $Q(z) = (x_p(z))max/(x_p(z))_{min}$ is the local ellipticity of the vacuum flux surface. The values of the weights A_{ei} and A_{ii} may be obtained by a simple analytic estimate or more accurately by numerically integrating the data from the magnetic field code MAFCO [8]. Results of such an integration are given below in Table 1.

Table I. A_{ei} and A_{ii} vs. M

M	Q_{max}	A_{ei}	A_{ii}
1	1	1	1
2	10	1.72	3.32
3	18	2.99	12.09
4	25	3.20	13.21

Equations (4a) and (5) taken together illustrate that the radial loss rate is enhanced by the ellipticity and reduced by higher mangetic fields as expected.

The ratio $\tau_\parallel/\tau_\perp$ may be evaluated for any mean free path regime by inserting the appropriate expression for $\tau_\parallel$ and rewriting Eq. (4) to express $\tau_\perp$ as

$$\frac{\tau_\perp}{\tau_{ii0}} = \frac{(\frac{m_i}{m_e})^{1/2} (\frac{x_{p0}}{a_{i0}})^2 (\frac{T_e}{T_i})^{1/2} (\frac{1}{A_{ei}})}{1 + 2(\frac{A_{ii}}{A_{ei}})(\frac{m_i}{m_e})^{1/2} (\frac{a_{i0}}{x_{p0}})^2 (\frac{T_e}{T_i})^{1/2}} \tag{6}$$

The denominator in Eq. (6) corrects for the higher order ion-ion contributions to the loss, which become comparable to the usual electron-ion losses when $(\frac{x_{p0}}{a_{i0}}) \sim (\frac{m_i}{m_e})^{1/4} (\frac{2A_{ii}}{A_{ei}})^{1/2}$.

The numerical model [2] has been used to calculate axial density profiles $n(z,t)$ (from which decay times may be inferred). The model is discrete in time and space with respective units ℓ_c/v (the single-cell

transit time of a mean energy particle) and ℓ_c. At any axial position the model follows the interaction of a trapped group of particles with two additional groups passing from the left and right. At every time iteration the density in each of the three groups is evaluated. Scattering between the groups is calculated based on the local value of the ion mean-free-path and a fraction of the particles is removed to account for the radial losses. The radial loss rates inserted into the code are calculated in manner similar to that discussed above. The modification of the loss-cone boundary and the subsequent effects on axial diffusion due to the ambipolar electric field is also accounted for in the model.

4. COMPARISON OF THEORY AND EXPERIMENT

The plasma centerline density $n(z,t)$ is monitored by means of an array of Langmuir probes arranged symmetrically about the center of the multiple-mirror at midplanes M_{12}, M_{34}, M_{45}, M_{56} and M_{78}. All probes are placed on axis and biased to collect ion saturation current. The temperature is determined in four independent measurements using (1) an ion energy analyzer, (2) a triple-probe, (3) a diamagnetic loop and (4) a single Langmuir probe technique. Results of several temperature measurements are presented in Table 2. The point-by-point Langmuir probe voltage scan (in the electron retarding region) is complicated by shot to-shot irreproducibilities introduced by the injectors and the data reduction is not straightforward since the electron gyro-radius is nearly the size of the probe radius. Nevertheless, the values are in good agreement with those obtained by direct measurement with an ion energy analyzer and those inferred from a diamagnetic loop. The triple probe

temperature measurements were only performed for a configuration without limiters for which the highest density measurements are taken. The temperature measured by this technique is also consistent with that found for the single probe. At higher magnetic fields the temperature is somewhat higher, owing to the reduction in radial plasma expansion between the theta-pinch and guide field.

Table II. Temperature Measurements

T_e: Langmuir Probes

Early in time ($n \sim 10^{13}$): $T_e \approx 8$ eV ± 2

Late in Time ($n \sim 10^{12}$): $T_e \approx 4$ eV ± 1

T_i: Ion Energy Analyzer

Early in Time ($n > 10^{13}$): $T_i \approx 7$ eV

Later in Time ($n \sim 3 \cdot 10^{12}$): $T_i \approx 5$ eV

$T_e + T_i$:

Diamagnetic Loop - Early Time: $T_{e\perp} + T_{i\perp} \approx 15$ eV

Density Decay in Solenoid

(from $\tau = \eta \frac{L}{v}$) [5] - Later Time: $T_e + T_i \approx 10$ eV

For Comparison With Theory

(late in time)

Assume $T_e = T_i = 5$ eV

The experimental loss mechanisms are characterized for several discrete density ranges in the following.

(a) High-density confinement (10^{14} - 10^{15} cm^{-3} with single-ended injection).

To measure the decay from the peak density, experiments were performed by injecting the theta-pinch plasma through rising mirror and quadrupole fields. The rising fields are crowbarred at a time nearly coinciding with the occurrence of peak density in M_{45}. Both limiters were removed. Four of the 2.2 µF theta-pinch capacitors were fired in a preionizer-series-crowbar mode. Densities and temperatures of $n \sim 10^{15}$ cm^{-3} and $T_e = T_i \approx 8$ eV could be obtained in the first few cells.

At these high densities and low temperatures the ion-ion mean-free-path and collision time are both very short ($\lambda_{ii}/\ell_c < 10^{-2}$, $\tau_{ii} < 10^{-1}$ µs) which suggests that this initial decay is due almost entirely to radial processes. Representative decay data are plotted in Fig. 3 and shown bracketed by two theoretical curves. Each curve is normalized to the data at $n \approx 10^{15}$ cm^{-3}. The curves are constructed by calculating the decay rate at a given density and using the extrapolated density at a neighboring time to calculate a new decay rate. The upper curve is obtained by setting $\tau = \tau_\perp$ with the prescription given in Eq. (6) and with the additional constraint that $A_{ei} = A_{ii} = 1$. This corresponds to the assumption that the radial loss is purely local so that diffusion at the midplanes is effectively decoupled from diffusion at the mirror throats. The averaging (along z) has been removed so that the plasma column is modelled as a long cylinder. This calculation should be appropriate when the radial loss times are much shorter than any axial drift or transit time of interest.

The lower curve is also calculated from Eq. (6) but here the integrals A_{ei} and A_{ii} are allowed to take on their full values. This case corresponds to the physical situation in which the radial confinement time is long or comparable to a single cell transit time. Individual ions sample the radial gradients along an entire cell length so that radial loss rates should be averaged as discussed in Section 3. Note that the experimental data is well represented at early times by the upper curve but then drops to a position bracketed by the two limits as the decay proceeds, probably indicating that a transition from local to global loss (in any mirror cell) occurs over this density regime. In these calculations the temperature is taken as 5 eV ($T_i = T_e = 5$ eV) and the plasma radius (at a midplane) as $x_{p0} = 3$ cm.

The calculations are only applied to the data at times after those corresponding to occurrence of peak density in M_{45} (see Fig. 3). Prior to that time, the plasma still possesses a large drift (Mach number ~ 1) and axial expansion. These phenomena are not accounted for in the above analysis. These two effects have been addressed in a separate paper on the dynamics of injection [9].

(b) Higher-intermediate density confinement (10^{13} - 10^{14} cm^{-3} with dual-ended injection).

In these experiments both sources were fired and both limiters were in place. The diameter of each limiter was adjusted to constrain the major diameter of the flux surface cross section at a mirror throat to equal the vacuum chanber I.D. Two theta-pinch capacitors were operated in a ringing mode. The Marshall gun was also allowed to ring.

Within the first few hundred microseconds after the sources fire

the plasma parameters fall into the high density MHD regime. Experimental decay data just after this time with n ~ 10^{13} - 10^{14} cm^{-3} is shown in Fig. 4 and is again bracketed by two limiting theoretical curves. Axial loss times are calculated to be $\tau_\parallel$ ~ 1 ms, so that, as before $\tau \approx \tau_\perp$ (given by Fig. 6). For each curve the temperature is taken to be 5 eV (T_i = 5 eV). The upper curve has x_{p0} = 3 cm and the lower curve x_{p0} = 2 cm. The fact that the data falls between these two limits may indicate that as λ_{ii} increases (with decreasing density) "clipping" at the mirror throats might more efficiently reduce the effective plasma radius throughout an entire cell. That is, charged particles on field-lines with midplane radii beyond a critical value will be lost to the vacuum chamber wall after traversing one-half of a cell length to the subsequent mirror throat. When the mean-free-path is small compared to a cell length this clipping at the throats is not effectively communicated to the adjacent midplanes.

(c) Intermediate density confinement (10^{11} - 10^{13} cm^{-3} with dual-ended injection).

Fig. 5 illustrates the general features of the confinement. Early in time the axial profile is peaked near the ends since the transmission of plasma from each injector to the device center is impeded by trapping in the intervening mirror cells. 400-500 μs after the sources are fired n(z,t) is nearly uniform in z. After this time the density has dropped to a value such that λ_{ii}/ℓ_c ~ 1 so that characteristic multiple-mirror normal modes begin to form (that is, the density profile peaks in the device center).

The experimental data are plotted against axial position in Fig.

6(a) at various times, beginning 400 µs after the sources are fired. At this time (for this particular shot) the density profile is weighted slightly toward the theta-pinch end of the device. Within the next 100 µs the density drops everywhere throughout the entire system and the slightly higher loss rate near the theta-pinch (M_{12}) has reduced the non-uniformity of the profile and allowed the initial formation of the normal mode to occur. By 600 µs the normal mode characteristic of the high-intermediate density regime is fully established, signalling the transition from radial-dominated to axial-dominated loss.

The ion-ion mean-free-path between the times 600 < t < 700 µs is .5 cm < λ_{ii}/ℓ_c < 1.2 cm. By 800 µs the appearance of concavity in the n(z,t) profile indicates that the plasma has made the transition into the lower-intermediate density regime. At 900 µs, $\lambda_{ii}/\ell_c \sim 2$ and the characteristic normal mode is fully established.

A numerical simulation, described briefly in Section 2 and in more detail in [2], is shown for comparison in Fig. 6(b). The initial condition n(z,t) = $1.5(10^{12})cm^{-3}$ is chosen to approximately correspond to the experimental profile at t = 400 µs. The normal modes characteristic of each regime are present but are slower to develop. The higher-intermediate density regime persists 700-800 µs after that time at which the profile is flat. This is to be compared with a corresponding time interval in the experimental case of 400-500 µs and is probably evidence that the theory underestimates the radial loss. (This will be discussed further in Section 5).

The measured (τ^{exp}) is compared with the analytical (τ^{anal}) and numerical (τ^{num}) confinement times for various mirror ratios (M) and

midplane field strengths (B_0) in Table 3. The calculated axial times (τ_{mm}^{anal}) are also listed. However, the axial and total times are comparable (within a factor of 2-3) indicating that radial processes do not dominate the loss in the intermediate mean-free-path regimes. The calculated times given in Table 3 are in all cases longer than the measured times. A possible explanation for the faster experimental decay is discussed in Section 5. The relative importance of radial and axial loss with variations in mirror ratio and field strength can be seen from the ratio $\tau_{mm}/\tau_{\perp}$ (calculated analytically) in Table 4. Along the main diagonal of the table, axial and radial processes are competitive. Toward higher (lower) mirror ratios and lower (higher) field strengths the radial (axial) losses dominate. The higher mirror throat flux surface

Table III. Confinement Time (μsec)

B_{0Ave} (kG)	1.1	1.6	2.1
Theory			
τ_{axial}	990	990	990
τ_{radial}	698	3060	8151
τ_{conf}	409	748	883
Simulation			
τ_{axial}	776	776	776
τ_{conf}	500	667	736
Experiment			
τ_{conf}	370	410	430

Table IV. $(\tau_{mm}/\tau_{\perp})^{anal}$ vs. M and B_0

	M = 2	3	4	
B_0(kG) = 1.1	.38	1.33	2.84	radial loss dominates
1.6	.08	.28	.61	
2.1	.03	.10	.21	
axial loss dominates			comparable	

ellipticities required for stability at higher mirror ratios introduce strong transverse gradients which enhance the radial diffusion. Specifically, as M and Q increase the critical midplane radius

$x_{p0} = x_{wall}(M/Q)^{1/2}$ decreases (see Table 1) thereby reducing the ratio

$(\frac{x_{p0}}{a_{i0}})$. Since $\tau_{\perp pi0} \sim (\frac{x_{p0}}{a_{i0}})^2$ and $\tau_{\perp ii0} \sim (\frac{x_{p0}}{a_{i0}})^4$ (see Eq. (4)) the radial

times shorten with increasing ellipticity. However, the axial time

$\tau_{mm} \sim M$ and the net result is a moderate increase in confinement with

increasing mirror ratio, as reflected by the measured times τ^{exp} in

Table 3. As B_0 decreases the gyro-radii increase thereby again reducing

the ratio $(\frac{x_{p0}}{a_{i0}})$. Since τ_{mm} is independent of the field strength the

confinement is expected to degrade with decreasing B_0.

5. DISCUSSION AND CONCLUSION

Three distinct transitions are observed while following the decay

from peak density. In the high-density regime (10^{14} - 10^{15} cm^{-3}) the

loss is almost entirely due to radial processes. At the highest

densities the decay is local, meaning that losses at the midplanes and adjacent mirror throats are decoupled. As the density drops, charged particles sample a larger region of the mirror cell during a decay time and the enhanced transport at the narrow throats affects the diffusion throughout the entire cell. A second transition for radial loss processes occurs in the higher-intermediate density regime (10^{13} - 10^{14} cm^{-3}). At the lower end of this range the mean-free-paths are sufficiently long that plasma loss at the mirror throats (due to fieldlines intersecting the walls) reduces the overall width of the radial distribution along the length of the cell. Plasma midplane radii are observed to approach the predicted values (less than 2 cm) from the anomalously large initial values (near 3 cm). Finally, in the intermediate density regimes (10^{11} - 10^{13} cm^{-3}) the radial transport grows sufficiently that the confinement is limited by axial loss.

The comparison of measured (τ^{exp}) and calculated times (τ^{anal} and τ^{num}) listed in Table 3 indicates that classical radial losses are nearly sufficient to account for the observed decay (provided both electron-ion and ion-ion collisions are included). The calculations overestimate the confinement time but the anomalous component of the radial loss is at worst comparable to the classical component. Furthermore, some portion of the error is due to several shortcomings and omissions in the theory, which are discussed below.

The analytical estimate assumes uniform density along the axis of the entire system. In the intermediate regime the reduced density near the end cells produces a higher rate of axial loss which is not accounted for in the analytical model. The numerical calculation does not suffer

this shortcoming. It calculates axial losses based on local (on axis) plasma parameters and for that reason (and the fact that it includes an ambipolar correction) provides a better approximation. Both calculations fail to account for the larger axial losses in plasma layers at larger radii (the onion-skin effect) and so would also be expected to under-estimate the loss for this reason. Enhanced transport due to micro-instabilities is not included. However a characteristic of the onion-skin effect is that high radial loss at the periphery (where the axial confinement is poor anyway) has little effect.

The most reasonable candidate to account for discrepancies between the numerical model and the experiment is fieldline misalignment. If the center fieldline at a midplane strays off axis at the mirror throat the effect will be to reduce the critical midplane radius. Small mis-alignments along the direction of the major-axis can produce significant reductions. The effect of local misalignments can extend over a large axial extent in the long mean-free-path regimes. Scaling of the mis-alignment with magnetic field and mirror ratio is tested in the follow-ing manner. The data in Table 3 is plotted in Fig. 7. The dotted curve in Fig. 7a is obtained by normalizing the results of the numerical model to the experimental value at the intermediate mirror ratio $M = 3$ and field strength 1.6 kG, and plotting the confinement time at the other values of B by assuming that fieldline misalignment is independent of B_0, i.e., the numerical curve in Fig. 7a is simply shifted downward. We see a close correspondence between the numerical and experiment scaling of the confinement time with B. In Fig. 7b the numerical values are similarly normalized and then scaled by the factor of $(\frac{M}{Q})$ which results from a fixed

mechanical misalignment. This again yields close agreement of the scaling of the measured and numerical curves as a function of M. The mechanical misalignment of the central field line was estimated from flux surface tracing with electron beams of the type shown in Fig. 2, and appears to be sufficient to account for the absolute decrease in confinement time. No attempt at an exact calculation of this effect was made.

In conclusion, for a stabilized multiple mirror device the density decay can be quantitatively accounted for by classical processes alone. This decay has been traced over four orders of magnitude, from the highest density of $n \approx 10^{15}$ cm^{-3} where radial loss dominates the decay to $n \sim 10^{11}$ cm^{-3} where the decay is dominated by axial loss. The decay in the multiple mirror regime for intermediate densities has been clearly seen.

REFERENCES

[1] Logan, B. G., Brown, I. G., Lieberman, M. A., Lichtenberg, A. J.,
     <u>Phys. of Fluids</u> 17 (1974) 1302.

[2] Tuszewski, M., Lichtenberg, A. J., Eylon, S., <u>Nucl. Fusion</u> 17 (1977)
     893; see also M. Tuszewski, "Experimental Study of Confinement and
     Stability in a Multiple Mirror," Ph.D. Thesis, University of
     California (1976).

[3] Tuszewski, M., Price, D., Lieberman, M. A., Bravenec, R., Doniger,
     K., Hartman, C., Lichtenberg, A. J., <u>Nucl. Fusion</u>, 19 (1979) 1244.

[4] Riordan, J. C., Lichtenberg, A. J., Lieberman, M. A., <u>Nucl. Fusion</u>
     19 (1979) 21.

[5] Taylor, J. B., Wesson, J. A., <u>Nucl. Fusion</u> 5 (1965) 159.

[6] Makhijani, A., Lichtenberg, A. J., Lieberman, M. A., Logan, B. G.,
     <u>Phys. of Fluids</u> 17 (1974) 1291.

[7] Tuszewski, M., Lichtenberg, A. J., <u>Phys. of Fluids</u> 20 (1977) 1263.

[8] Perkins, W. A., Brown, J. C., UCRL-7744-Rev. II, (1966).

[9] Bravenec, R. V., Lichtenberg, A. J., Lieberman, M. A., "Axial plasma
     injection and shock formation in multiple mirrors," <u>Phys. of Fluids</u>,
     to be published; see also R. V. Bravenec, "Axial flow of a colli-
     sional plasma through multiple magnetic mirrors," Ph.D. Thesis,
     University of California (1982).

[10] Steinhauer, L., <u>Physics of Fluids</u> 19 (1976) 738.
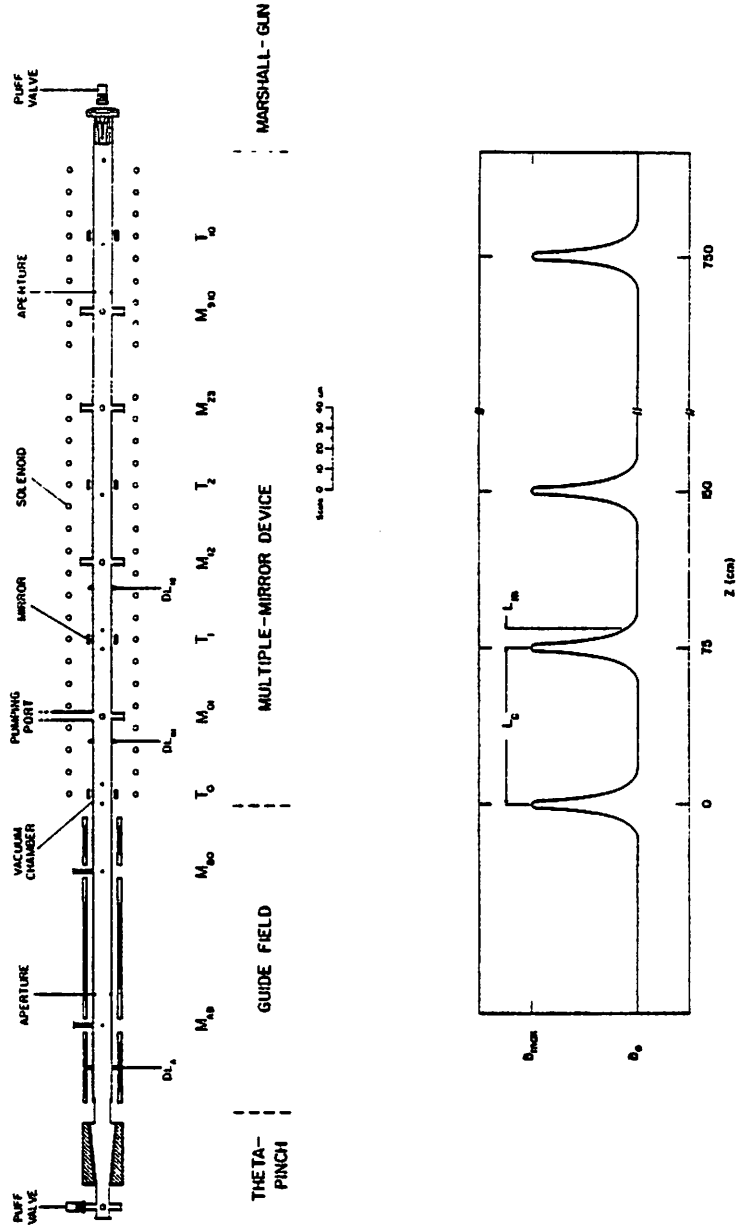
Fig. 1. (a) Schematic of the 10 meter multiple-mirror device.
(b) Axial magnetic field profile.
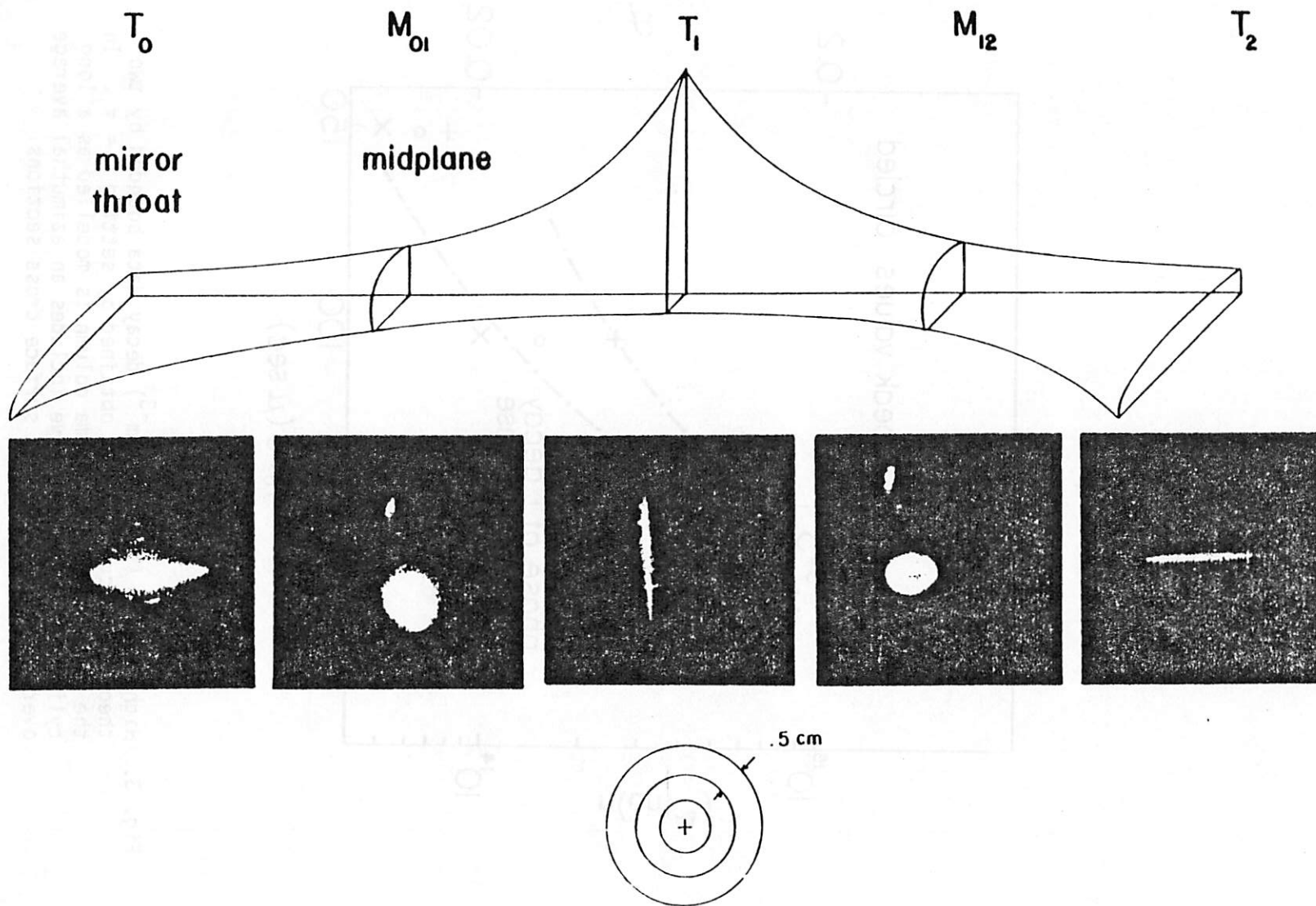
Fig. 2. Flux surface schematic and actual flux surface cross sections mapped by an electron beam source and photographed with the plasma camera.
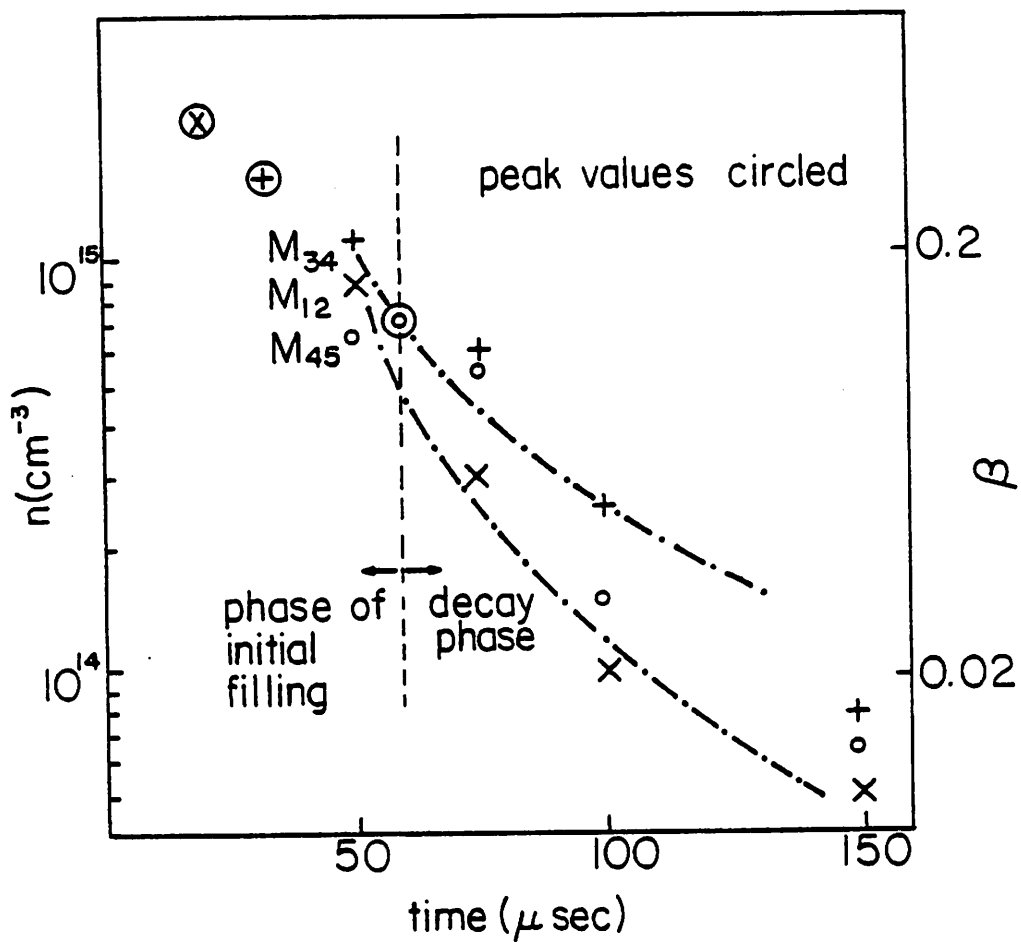
Fig. 3. High density (10^{14}-10^{15}cm^{-3}) decay data bounded by two theoretical curves, each obtained by setting $\tau = \tau_\perp$. In the upper curve the plasma column is modelled as a long cylinder. The lower curve includes an azimuthal average over the elliptical flux surface cross sections.
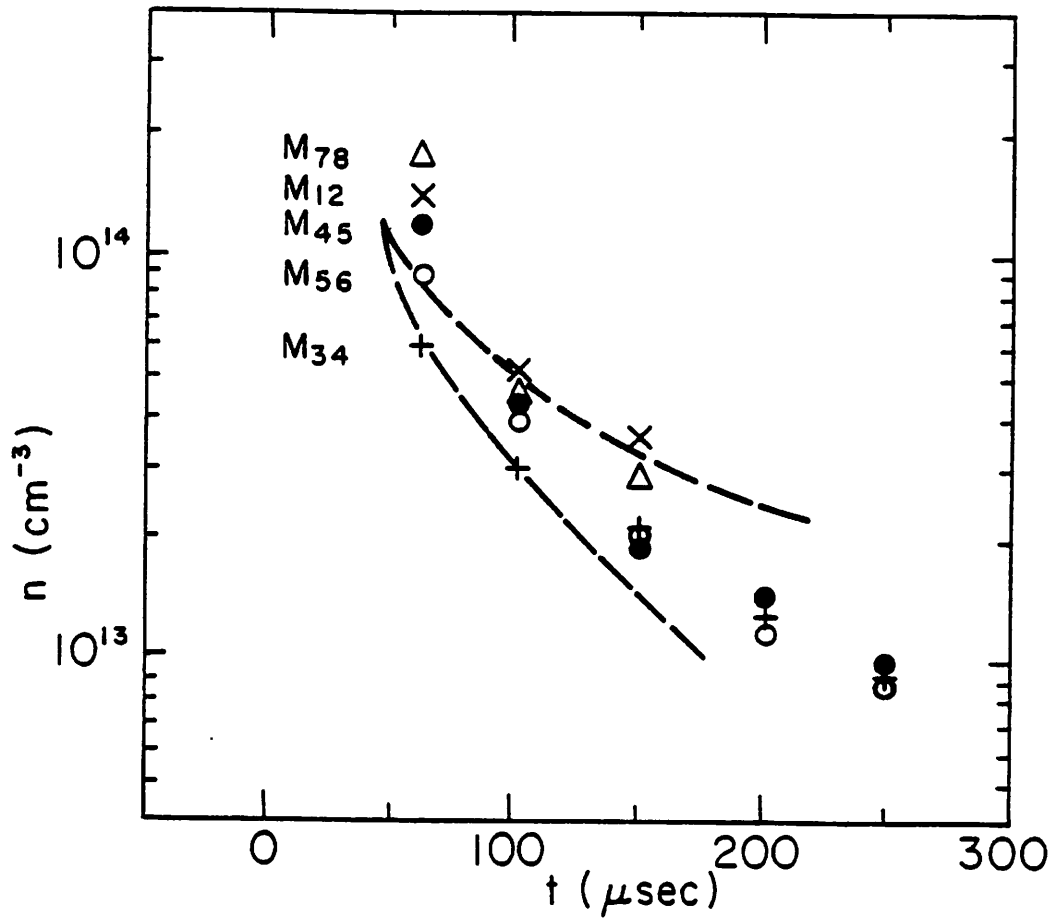
Fig. 4. Higher-intermediate density (10^{13}-10^{14} cm^{-3}) decay bounded by two theoretical curves, each obtained by setting $\tau = \tau_\perp$. The upper curve assumes a plasma radius of 3 cm and the lower curve assumes a plasma radius of 2 cm.
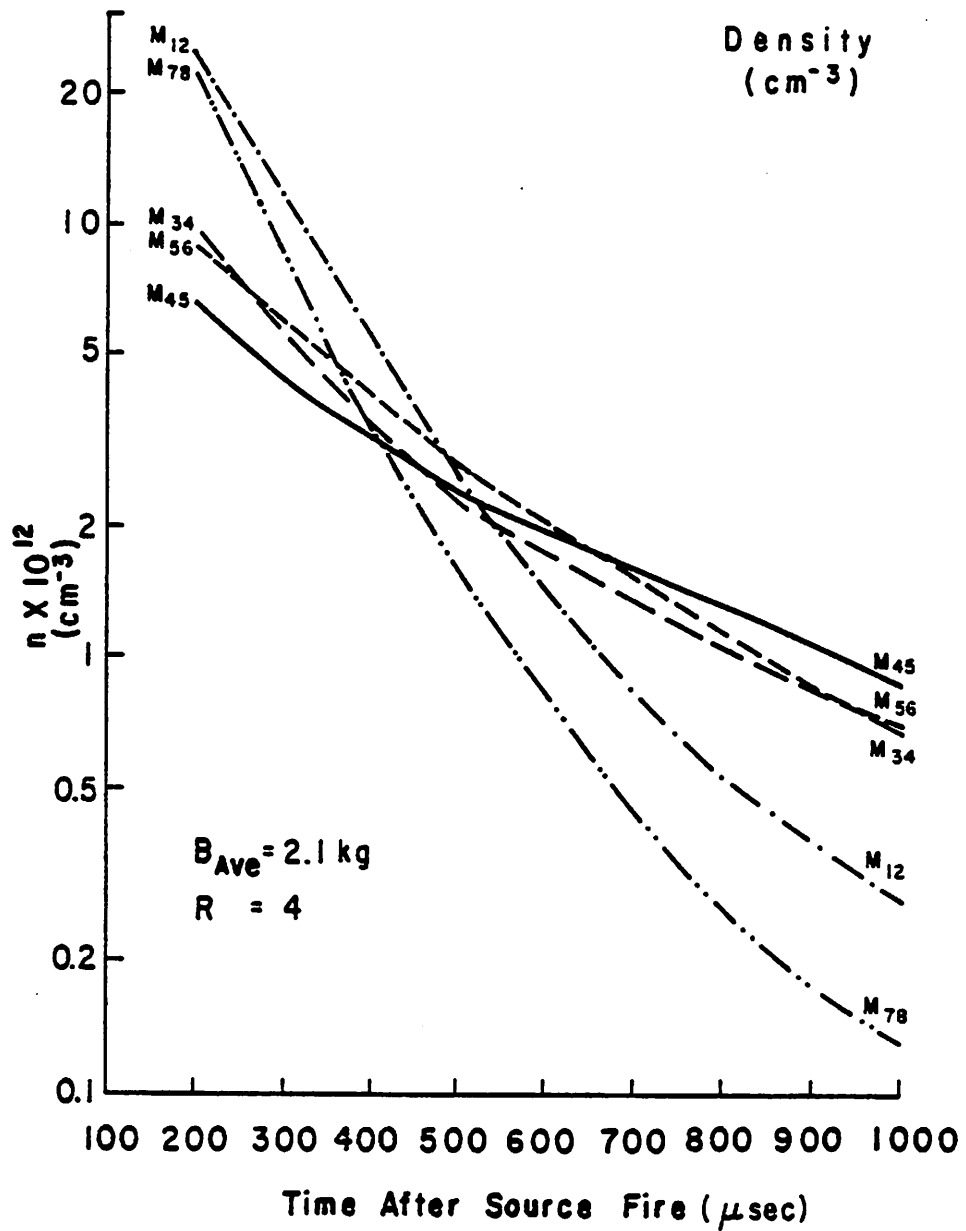
Fig. 5. Intermediate density (10^{11}-10^{13} cm^{-3}) decay data obtained from an axial array of Langmuir probes.
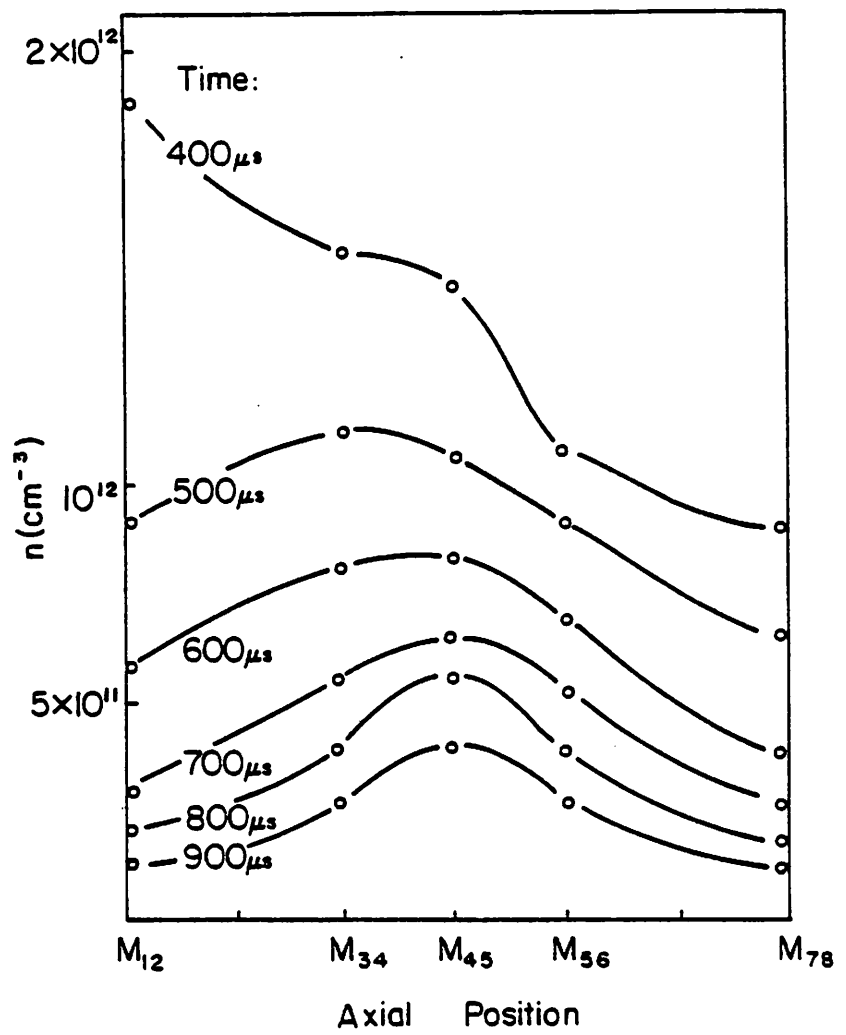
Fig. 6. (a) Normal mode formation, experimental data.
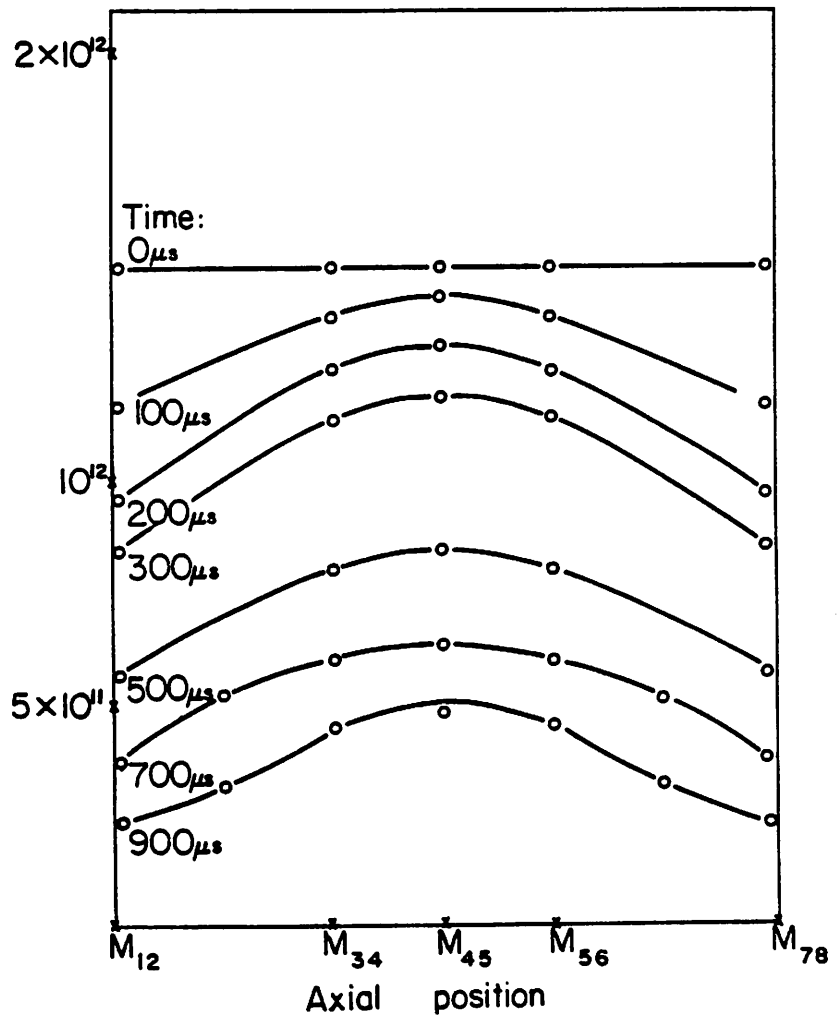
Fig. 6. (b) Normal mode formation, numerical data.
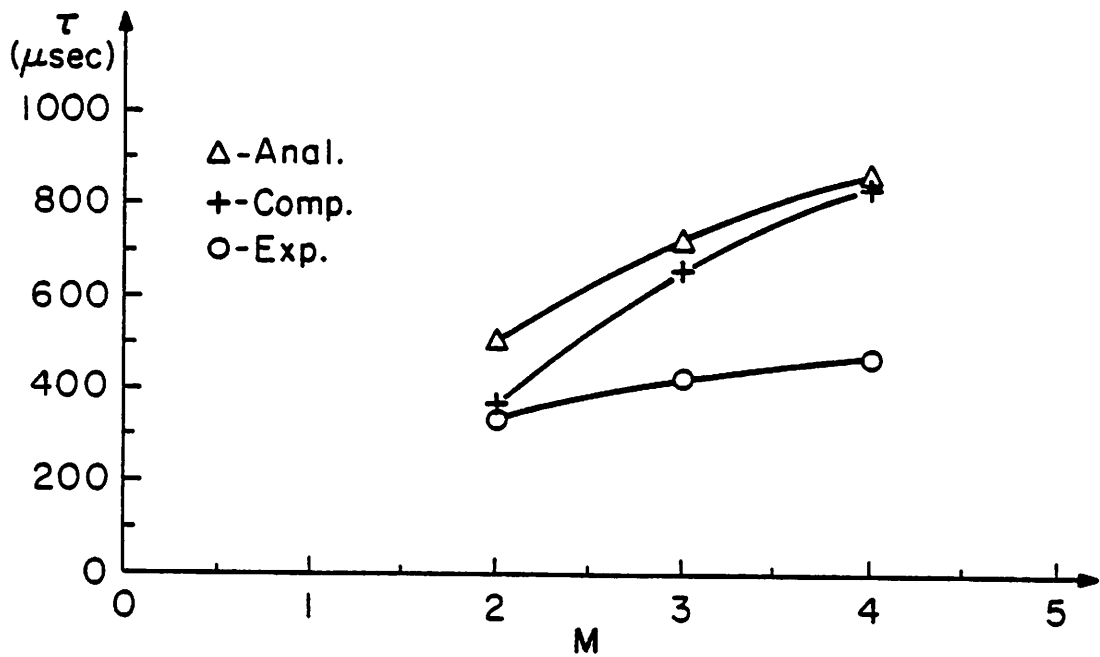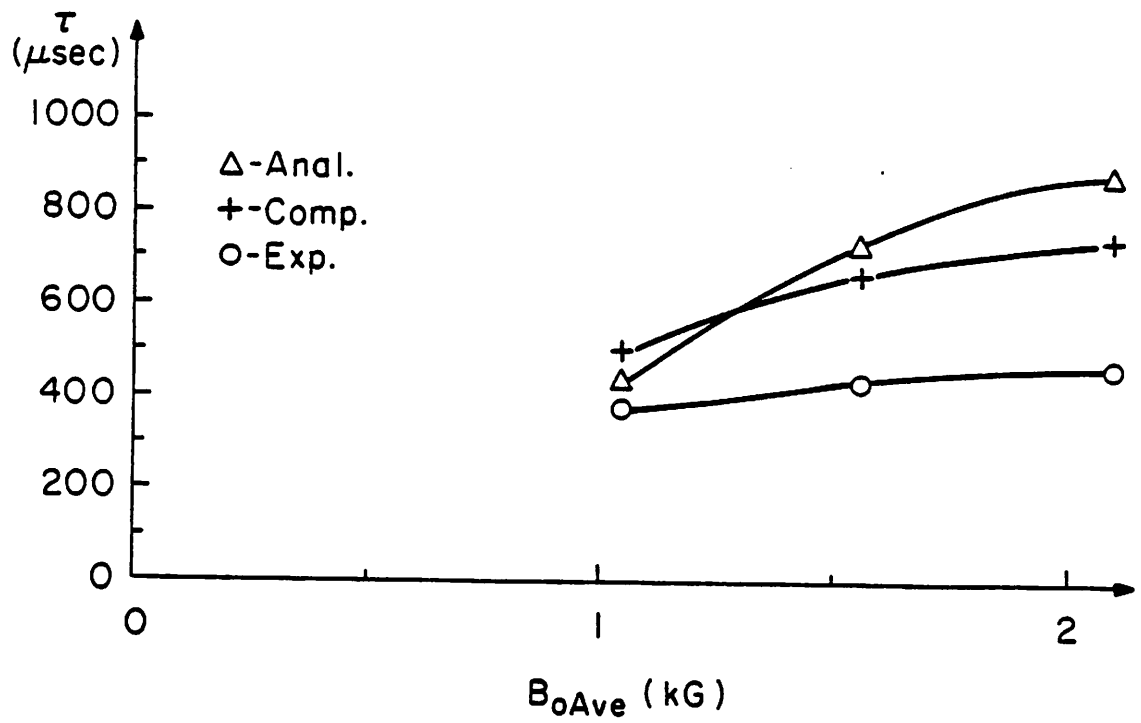
Fig. 7. Overall confinement time vs. (a) midplane field strength B_o and (b) mirror ratio M.